Surface Heterogeneity and Diffusion in the Desorption of Methanol from WO_3(001) Surfaces

S. Ma,[†,‡] F. G. Amar,[†] and B. G. Frederick*[,†,‡]

Department of Chemistry and Laboratory for Surface Science and Technology, University of Maine, Orono, Maine 04469

Received: October 15, 2002; In Final Form: December 10, 2002

We have investigated the role of intermolecular interactions, surface site heterogeneity, and surface diffusion on the desorption of methanol from the oxidized and reduced surfaces of (001) oriented, epitaxially grown WO_3 films on $Al_2O_3(\bar{1}102)$ substrates. Ultraviolet photoelectron spectroscopy (UPS) showed that methanol adsorbed molecularly on the oxidized WO_3 surface but dissociatively on the reduced surface. On both surfaces, calibrated thermal desorption spectroscopy (CTDS) showed the desorption of methanol as an asymmetric peak that shifts to lower temperature with increasing coverage, behavior that is typical of water and alcohols on other oxide surfaces. X-ray photoelectron spectroscopy (XPS) was used to characterize the surface by monitoring the W4f and valence-band region; STM studies indicate that the surface is heavily stepped. Monte Carlo simulations including surface heterogeneity and rapid diffusion effects are consistent with the observed desorption spectra.

I. Introduction

Desorption from surfaces is a well-known and fundamental phenomenon in catalysis, widely used to study the energetics and kinetics of adsorption, desorption, and surface chemistry.[1] Although desorption spectra on metals typically focus on the decomposition reactions and desorption kinetics, the desorption process can be controlled by additional factors. These include surface diffusion, the surface heterogeneity, and the interaction between adsorbates, depending on the chemical properties of the adsorbates and the surface structures of the adsorbent.

The adsorption and desorption of methanol on different metal oxide surfaces have been extensively studied[2−8] as the simplest alcohol, as a probe molecule for surface acidity, and as an important reagent for the production of formaldehyde. The desorption of methanol is usually characterized by a large temperature span and a long tail on the high-temperature side.[3,6,7] Surface diffusion, interactions between adsorbed methanol molecules, and the surface adsorption site heterogeneity may all play a role in producing this desorption profile. The surface heterogeneity results from metal oxides' sensitivity to the surface treatment and subsequent defect formation such as oxygen vacancies and stepped structures.

Similar desorption features are widely observed for water adsorption on metal oxide surfaces.[9−15] However, there are only a few detailed studies of the role of the microscopic factors involved in the desorption process.[13−15] Most previous theoretical simulations of desorption were limited to simple diatomic molecules on homogeneous metal surfaces assuming fast surface diffusion.[16,17]

In this paper, we study the adsorption and desorption of methanol on the sapphire single-crystal supported WO_3(001) surfaces using calibrated thermal desorption spectroscopy (CTDS)[18] combined with Monte Carlo simulations to explore the role of the surface heterogeneity, the interaction between the adsorbates, and the surface diffusion of adsorbates during desorption.

Pure WO_3 is a good insulator; however, it has been thoroughly studied as a semiconducting material[19−22] since defects, particularly oxygen vacancies and crystallographic shear planes, can easily create variable tungsten oxidation states. In our laboratory, WO_3-based sensors have been studied for potential use in nerve agent (sarin and taban) detection[23,24] using dimethyl methylphosphonate (DMMP) and other organophosphonates as simulants of these warfare agents.[25] The decomposition and loss of methoxy groups on WO_3 is similar to the surface chemistry of DMMP on other metal oxide surfaces.[26−30] However, knowledge of the decomposition products of the methoxy groups and details of the reaction mechanism on most surfaces are limited. To interpret the decomposition and reaction mechanism of DMMP on the WO_3 surface,[31] it was necessary to study the surface chemistry of methanol on WO_3. This also motivates the present study.

The experiments were performed on two different kinds of surfaces: the gently sputtered surface and the surface oxidized in oxygen after sputtering. X-ray photoelectron spectroscopy (XPS) was used to characterize the surface by monitoring the W4f and the valence-band regions. Ultraviolet photoelectron spectroscopy (UPS) was used to monitor the adsorption state of methanol on the WO_3(001) surface. Calibrated thermal desorption spectroscopy (CTDS) was used to monitor the reaction products and quantify the absolute coverage during the desorption processes. This study shows that surface heterogeneity and diffusion play important roles in the desorption of methanol. As far as the surface reaction was concerned, no other reaction products, for instance, dimethyl ether, were detected.

II. Methods

II. A. Experimental Methods. The WO_3 thin films were grown epitaxially on the single-crystal α-$Al_2O_3(\bar{1}102)$ substrate

* Corresponding author. E-mail: brian.frederick@umit.maine.edu. Tel: (207) 581-2268. Fax: (207) 581-2255.
† Department of Chemistry.
‡ Laboratory for Surface Science and Technology.

10.1021/jp0222292 CCC: $25.00
Published on Web 02/11/2003

by RF magnetron sputtering of a pure tungsten target in a 50/50 oxygen/argon atmosphere at a total pressure of 4×10^{-3} mbar in a thin film deposition system.[32] The 500-Å films were grown at 1 Å/s with the substrate held at 773 K. The structure of the film and the surface morphology have been studied[32,33] using reflection high-energy electron diffraction (RHEED), X-ray diffraction (XRD), transmission electron microscopy (TEM), and scanning electron microscopy (SEM).

All of the spectroscopic experiments were performed in a separate stainless steel vacuum chamber, which was pumped by a turbo molecular pump and an ion pump to a base pressure of 5×10^{-10} mbar. The system is equipped with a differentially pumped mass spectrometer, sputtering gun, concentric hemispherical electron energy analyzer, dual-anode X-ray source, and differentially pumped UV lamp.

The mass spectrometer (Balzers QMG 112 A) is mounted in a cylindrical shroud, which is coaxial to the ionizer and quadrupole. The shroud extends to a translatable conical shroud in front of the ionizer with a 3.63-mm-diameter aperture at the end. A second turbo molecular pump (360 L/s) was used separately to pump the mass spectrometer housing. The shroud geometry was designed[18] so that the following properties were achieved: (1) a linear relationship between the pressure in the ionizer and the mass spectrometer signal over 4 orders of magnitude; (2) sensitivity to 10^{10} molecules/(cm^2 s) flow rates ($\sim 10^{-5}$ monolayer); (3) a time constant of approximately 6 ms for inert gases; and (4) a large "pumping-speed immunity" (i.e., a weak dependence of the ionizer region pressure to changes in the pumping speed at the turbo pump inlet).

The $WO_3/Al_2O_3(\bar{1}102)$ sample was mounted on a 1-cm^2 tantalum block by spot welding thin tantalum foil strips over the edges of the sample. The tantalum block was then spot welded to 0.5-mm-diameter Ta wires, which were welded to Ta rods. The rods were electrically isolated from a liquid nitrogen-cooled copper block by a sapphire wafer (0.7 mm thick).

The sample could be resistively heated to 800 K and cooled to 140 K with this design. A K-type (nickel−chromium vs nickel−aluminum) thermocouple was spot welded on the back of the tantalum block to monitor the sample temperature.

A microchannel array doser is aligned with the mass spectrometer. The doser is connected through a positive shutoff (PSO) valve to a known-volume gas cell whose pressure is monitored by a spinning rotor gauge. The effusion rate of the PSO valve (10^{13} molecules N_2/s at 10^{-3} mbar) provides a flow rate comparable to the desorption rate in a typical desorption experiment. This dosing system can be used to calibrate the mass spectrometer, for compounds that do not stick to the doser, by monitoring the pressure in the gas cell versus time.[18]

For sticky gases, the calibration of the mass spectrometer required a more complicated procedure. The flux impinging on the entrance aperture of the mass spectrometer shroud, $\Gamma = P/\sqrt{2\pi mkT}$ given by the kinetic theory of gases is valid at the pressures utilized here. We assumed that the detector current, $I^{\mathrm{SEM}} = I^{\mathrm{F}}G$, is proportional to the flux, $I^{\mathrm{SEM}} = c\Gamma$, where I^{F} is the current measured with the Faraday plate and G is the SEM gain. Thus, the calibration factor, $c = (I^{\mathrm{F}}/P)G\sqrt{2\pi mkT_{\mathrm{cal}}}$, for a given mass fragment (at the chamber calibration temperature T_{cal}) includes the pumping speed through the ionizer (at the calibration temperature), the ionization cross section, and the mass spectrometer's transmission efficiency. The detection efficiency is included in the gain, measured on a day-to-day basis.

During adsorption, the surface was cooled to 140 K and positioned 1−2 mm away from the doser, where the flux is uniform.[18] After dosing, the sample was rotated toward the mass spectrometer cone and positioned within 1 mm before starting the desorption experiment. Therefore, interference due to desorption from the wall, the edge of the tantalum block, and the manipulator can be ruled out. CTDS data were acquired under computer control, recording up to eight masses.

The major contaminant on the surface, after introducing the sample to the analysis chamber, was carbon. XPS showed a rather strong C 1s peak before cleaning. The WO_3 surface was cleaned by Ar^+ sputtering (100-μA beam current, 500 eV) until the C 1s signal was reduced below the XPS detection limit. Meanwhile, sputtering preferentially removed lattice oxygen, resulting in the "reduced surface". The sputtered surface was treated in oxygen at approximately 0.2 mbar and 300 °C for 2 h to produce the "oxidized surface".

UPS and XPS measurements were made at normal emission with a hemispherical analyzer (Leybold EA-10). For XPS, the Mg Kα source (Perkin-Elmer, Φ 32-095) was operated at 15 keV and 100 W, incident at 45° with respect to the surface normal. The pass energy was fixed at 20 eV for detailed scans and at 100 eV for survey scans. For UPS measurements, a UV lamp (Leybold UVS 10/35) produced He(II) radiation (40.8 eV) incident at 45°, and measurements were made at a pass energy of 10 eV, corresponding to a resolution of 0.2 eV.

Curve fittings of XPS spectra were performed with the freeware XPSPEAK 4.0 by Kwok using the sum of Gaussian and Lorentzian functions as the model function. During fitting, the peak area ratio of $W4f_{5/2}$ to $W4f_{7/2}$ was constrained to 0.78 on the basis of the calculated cross sections by Scofield,[34] and the spin−orbit splitting was fixed at 2.1 eV.

Oxygen (99.997%) and argon (99.9996%), both from Airco Specialty Gases, were used for oxidizing and sputtering the surface, respectively. Methanol (EM Science, >99.8%) was purified using freeze−pump−thaw cycles. The mass spectrum of the further purified methanol sample showed that the rise in the intensity at mass 18 due to water was less than 12% of the intensity at mass 31 of the most intense methanol fragment and that significant peaks due to other compounds were not observed.

II. B. Theoretical Methods. We now describe the Monte Carlo model developed for the simulation. The catalytic surface was represented by a square L × L lattice of adsorption sites with periodic boundary conditions. The desorption rate for a molecule in the type i local adsorption configuration is given by

$$\mathrm{rate}_i = \nu_{d,i} \exp\left(-\frac{E_{d,i}}{k_{\mathrm{B}}T}\right) \tag{1}$$

where $\nu_{d,i}$ is the preexponential factor and $E_{d,i}$ is the activation energy of desorption, which is defined by

$$E_{d,i} = E_{d,i}{}^0 + N_{nn,i}\,E_{nn} \tag{2}$$

Here, $E_{d,i}{}^0$ is the activation energy for the desorption of an isolated molecule from site i, $N_{nn,i}$ is the number of nearest-neighbor adsorbates of the ith molecule, and E_{nn} is the interaction energy between nearest neighbors. Only the nearest-neighbor interaction was considered in these simulations. The sign convention made for E_{nn} is that E_{nn} is positive for attractive interactions and negative for repulsive interactions. In the simulation, the preexponential factor $\nu_{d,i}$ was assumed to be identical for all of the adsorbates with different local configura-

tions. For a homogeneous surface model, all $E_{d,i}^0$ are identical, whereas for a heterogeneous surface model, the $E_{d,i}^0$ values were randomly chosen from a distribution. For example, for a normal distribution, the mean $\bar{E}_d$ and standard deviation ΔE parametrized the distribution.

Diffusion and desorption were treated as two competitive surface processes. We controlled the relative diffusion and desorption rates by introducing a parameter $r = R/(R + 1)$, where R is the ratio of diffusion attempts to desorption attempts and $0 < r < 1$. This definition of r means that the probability of diffusion is higher for large r. R is in principle determined by the difference in the activation energy between diffusion and desorption processes.

The Monte Carlo algorithm is formulated as follows:

(1) Randomly populate the L × L lattice sites with N_0 adsorbates at the initial surface coverage θ_0 ($\theta_0 = N_0/L^2$) and initial temperature T_0.

(2) Randomly choose a molecule on the lattice. Select a random number between 0 and 1, and attempt diffusion if it is less than r, or attempt desorption otherwise. For the diffusion test, step 3 will be performed, whereas for the desorption test, step 4 will be conducted.

(3) For the diffusion test of a chosen molecule, randomly choose a nearest-neighbor site. If it is occupied, return to step 2. If it is empty, then the molecule jumps into the new site if a random number between 0 and 1 is less than $\exp(-\Delta E/kT)$, where an energy difference, $\Delta E < 0$, corresponds to a favorable jump between the chosen nearest-neighbor site and the initial site. Then return to step 2.

(4) For the desorption test, the desorption probability was calculated by

$$p_{d,i} = \nu_{d,i} \exp\left(-\frac{E_{d,i}}{kT}\right)\Delta t \qquad (3)$$

where the time step Δt was decreased until the shape of the spectrum converged. A linear program was used for the temperature $T = T_0 + \beta\Delta t$, where β is the ramp rate. Desorption occurs if a random number between 0 and 1 is less than $p_{d,i}$. The desorption tests were counted by a parameter, m_{trial}, that was set equal to the number of adsorbates on the lattice at the beginning of each temperature step, and m_{trial} was decreased by 1 for each desorption attempt (whether a desorption event occurs or not). Once m_{trial} desorption attempts were tested, the temperature was increased by $\Delta T = \beta\Delta t$. Since the diffusion test does not affect the rate that the surface temperature increases, the ratio R controls the extent to which surface equilibrium can be established. The desorption rate was calculated by $R = \Delta N/\Delta t$, where ΔN is the number of molecules that desorb. The simulation was conducted in MathCad version 2000. Initial simulations utilized lattices with 100 × 100 sites, but larger 200 × 200 lattice sizes were then used for production runs. The time step was varied between 0.1 and 0.5 s to test the convergence of the algorithm. For $\Delta t \geq 0.5$ s, significant peak shifts were observed; therefore, a time step of $\Delta t = 0.2$ s was utilized for the spectra shown. Comparisons were also made to the direct numerical solution of the corresponding Polanyi−Wigner equation for appropriate cases (i.e., in the rapid diffusion limit).

III. Results

III. A. Experimental Results. Characterization of the WO_3 Films after Initial Growth. Previous studies in our laboratory show that the structure, the stoichiometry, and the electrical properties of WO_3 films grown on *r*-cut sapphire substrates are very sensitive to the growth conditions. Reflection high-energy electron diffraction (RHEED) in transmission and glancing incidence X-ray diffraction (XRD) show that the WO_3 films made at the conditions described above are grown in the highly oriented monoclinic phase with the (001) planes (of the nearly cubic structure) parallel to the sapphire substrate surface.[32,33,35] Scanning electron microscope (SEM) images of the cleaved edge of the film show that the film, as deposited, is very dense, whereas TEM measurements indicate that pores, if present, are less than 1 nm in width.[33] However, heavily stepped structures and domains were observed in scanning tunneling microscope (STM) images.[32] Annealing in oxygen at high temperatures can smooth the surface significantly.[32] Before CTDS experiments, the surface was heated at 4 K/s to 800 K in vacuum several times until no desorption was observed.

XPS Characterization of the WO_3(001) Surfaces. Two types of surfaces were produced for this study: the sputtered surface and the oxidized surface, which was produced by treating the sputtered surface in oxygen at high temperature. XPS was employed to characterize these surfaces by analyzing the W4f and valence-band regions.

Two types of oxygen exist on the bulk terminated (001) surface: terminal oxygen and bridging oxygen. Figure 1A shows the structure of monoclinic WO_3. Because the deviations from the cubic ReO_3 structure are very small ($\beta = 90.9°$; $a = 0.730$ nm, $b = 0.754$ nm, $c = 0.769$ nm),[36,37] the (001), (010), and (100) orientations are present in the epitaxial film; however, the (001) face is prevalent.[32] As in previous single-crystal studies,[38,39] we refer all surface structures to the idealized cubic structure and make no distinction between the (100), (010), and (001) surfaces. In the nonpolar c(2 × 2) surface, shown in Figure 1B, half of the terminal oxygens are removed to produce a stable, charge-neutral surface.[22,40] Sputtering may preferentially remove oxygen, either in the terminal or bridging positions, to result in a reduced, disordered surface. Formally, the five-coordinate tungsten cations, with missing terminal oxygens, are in the 5+ oxidation state. However, annealing the surface would also be expected to produce shear plane structures, which also result in reduced formal cation oxidation states. At shear plane boundaries (see Figure 1C) in which an octahedron has two corner-sharing and two edge-sharing octahedra neighbors, the cations would also be in the 5+ formal oxidation state. Removal of the terminal oxygen from the cation at the shear plane would formally produce a 4+ oxidation state.

Figure 2A shows a W4f XPS spectrum for the epitaxially grown film following introduction to the analysis chamber. Only the W^{6+} spin−orbit doublet contributes to the spectrum. The W4f XPS spectra for the ion-sputtered or thermally treated surfaces (Figure 2B−D) are complicated by the emergence of new bands in the lower binding energy region, whose intensity depends on the extent of surface treatments. At present, two mechanisms have been proposed to interpret the W4f spectrum.

The first mechanism, which originates from many-body effects, supposes that, when the electrostatic interaction between the core hole, after photoionization, and an electron in the conduction band[41] is strong enough to exceed the width of the conduction band, the conduction-band state can be pulled down into the gap to form a localized state, trapping the conduction electron. Two final states can be evolved, depending on the occupancy of the localized state; if the trap is occupied, final-state screening results in a lower apparent binding energy (i.e., the "screened" final state) compared to that of the "unscreened"

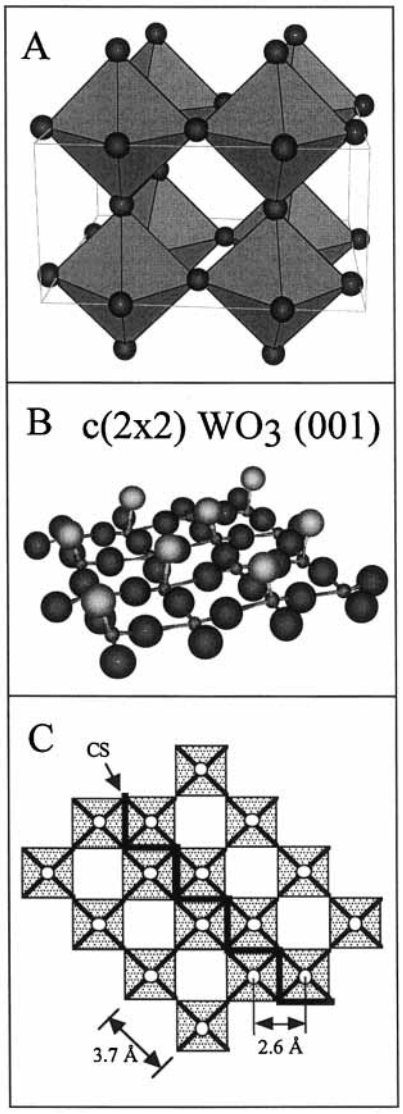

Figure 1. (A) Structure of monoclinic WO_3 shown as a corner-sharing octahedra. Small tilting and distortions of the octahedra result in the W_4O_{12} unit cell shown. (B) Model of the c(2 × 2) nonpolar structure WO_3(001) surface (periodicity referenced to the idealized, cubic ReO_3 structure). (C) Illustration of the approximately 3.7-Å W−O−W distances in the WO_3(001) face and the shorter (∼2.6-Å) W−W distances at crystallographic shear (CS) boundaries (indicated by the heavy line).

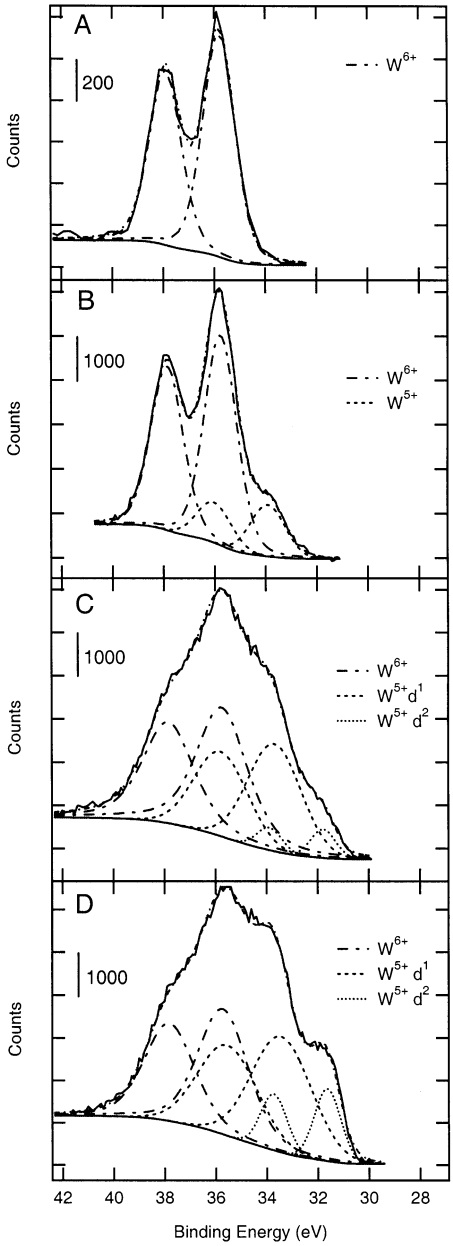

Figure 2. (A) W4f XPS spectrum of a fully oxidized WO_3 film (solid line) after growth and introduction to the analysis chamber. (B) Spectrum for a WO_3 film after sputtering and oxidation in 0.24 mbar O_2 at 300 °C for 2 h fit with W^{6+} and W^{5+} d^1 final-state spin−orbit split doublets (dashed curves). (C) Spectrum of an Ar^+ sputtered (500 eV, 100-μA beam current, 110 s) WO_3 surface fit with W^{6+}, W^{5+} d^1, and W^{5+} d^2 final-state spin−orbit split doublets (dashed curves). (D) Spectrum of a heavily sputtered surface fit with W^{6+}, W^{5+} d^1, and W^{5+} d^2 final-state spin−orbit split doublets (dashed curves). The peak parameters for fits to the final and initial state models are given in Tables 1 and 2, respectively.

final state in the case when the trap is empty. For this mechanism, two final states are possible from the same initial oxidation state, and the relative intensity and shift are dependent upon the electron density near the Fermi level.[42]

The second mechanism assigns the features to different initial states. Lower oxidation state tungsten species are assigned to W^{5+} and W^{4+}, following mild ion sputtering or thermal treatment and, additionally, to metallic W^0 from extensive sputtering.[20,43−46] Hence, in this mechanism, the W4f spectrum is fit with up to four different spin−orbit doublets representing different *initial* states (formally W^{6+}, W^{5+}, W^{4+}, and W^0).

The final-state screening mechanism has been favored for the interpretation of core-level XPS spectra for sputtered and annealed WO_3(001) single-crystal surfaces that were also characterized by LEED and STM.[39] Dixon et al.[39] found that significant differences above the valence band (i.e., in the gap of stoichiometric WO_3), as measured with UPS, could be correlated with formation of "troughs" running across the c(2 × 2) terraces and regions of high tunneling probability ("bright rafts") on more reduced surfaces.[39]

Figure 2B−D shows W4f XPS spectra for the oxidized, reduced, and heavily sputtered surfaces, respectively. We note first that the spectra can be fit in a manner consistent with both the final-state screening mechanism and the initial-state model. The spectrum of the oxidized surface, shown in Figure 2B, was fit with two spin−orbit doublets assigned to the d^0 final state of W^{6+} ($W4f_{7/2}$ BE = 35.8 eV) and the unscreened d^1 final state of W^{5+} ($W4f_{7/2}$ BE = 33.9 eV). The spectra in Figure 2C and D were fit with three spin−orbit doublets assigned to the

TABLE 1: Parameters Obtained from Fitting the Final-State Model

surface studied	oxidation state	binding energy ($W4f_{7/2}$) (eV)	fwhm (eV)	surface composition (%)
as-grown	W^{6+}	35.7	1.46	
oxidized	W^{5+}	33.9	1.61	19
after	W^{6+}	35.8	1.50	81
sputtering				
reduced	W^{5+} d^2	31.8	1.15	
	W^{5+} d^1	33.7	2.46	44
	W^{6+}	35.7	2.36	56
heavily	W^{5+} d^2	31.6	1.21	
reduced	W^{5+} d^1	33.4	2.76	55
	W^{6+}	35.7	2.33	45

TABLE 2: Parameters Obtained from Fitting the Initial-State Model

surface studied	oxidation state	binding energy ($W4f_{7/2}$) (eV)	fwhm (eV)	surface composition (%)
as-grown	W^{6+}	35.7	1.46	
oxidized	W^{4+}	33.8	1.52	18
after	W^{5+}	35.5	1.52	20
sputtering	W^{6+}	35.8	1.46	62
reduced	W^0	31.7	1.02	10
	W^{4+}	33.7	2.34	34
	W^{5+}	35.5	2.10	11
	W^{6+}	35.8	2.40	45
heavily	W^0	31.6	1.12	29
reduced	W^{4+}	33.7	2.59	29
	W^{5+}	35.6	2.25	17
	W^{6+}	35.8	2.44	25

d^0 final state of W^{6+} ($W4f_{7/2}$ BE = 35.7 eV), the unscreened d^1 final state of W^{5+} ($W4f_{7/2}$ BE = 33.7 eV), and the screened d^2 final state of W^{5+} ($W4f_{7/2}$ BE = 31.8 eV). The results of the final-state model are given in Table 1. Small contributions from the W 5p level were neglected.[42]

The W4f XPS spectrum shown in Figure 2B can be fit equally well with three doublets (cf. two in the final-state model) assigned to W^{6+}, W^{5+}, and W^{4+} on the basis of the initial-state mechanism. Likewise, the spectra in Figure 2C and D can be fit with four doublets (cf. three in the final state model) assigned to W^{6+}, W^{5+}, W^{4+}, and metallic W^0. These fits are not shown, but the results are given in Table 2.

Valence-band spectra, measured with He(II) radiation, compare very well in shape and relative intensity to data shown by Dixon et al.[39] The UPS valence-band spectrum corresponding to our Figure 2B is essentially identical to the spectrum in Figure 9a of ref 39 for the c(2 × 2) surface with troughs (the STM image in Figure 2a of ref 39), whereas that corresponding to our Figure 2C is very similar to the UPS spectrum in Figure 12a of ref 39 for their sputtered and annealed surface (and the STM image shown in Figure 2b of ref 39). The similarity of our XPS and UPS data to that of Dixon et al. and estimates of the substoichiometry, x, in WO_{3-x} based upon considerations given by Chazalviel et al.[42] lead us to favor the final-state model for reasons discussed further below. Regardless of interpretation, the spectra of Figure 2B and C and corresponding UPS valence-band regions uniquely characterize the surfaces that were used for the methanol adsorption and desorption experiments.

Adsorption State of Methanol on WO_3(001) Surfaces. UPS is a convenient technique with which to study the adsorption state of methanol. Five bands can be identified for the molecular adsorption of methanol in UPS using a He(II) source; these are assigned to the 2a″, 7a′, 6a′, 1a″, and 5a′ molecular orbitals within the C_s point group.[47] If a methoxy group with higher, C_{3v} symmetry is formed via the dissociation of methanol, then the 2a″and 7a′ and the 1a″ and 5a′ orbital pairs become degenerate; these are assigned to the 2e and 1e orbitals, respectively, and 6a′ is designated as the totally symmetric $5a_1$ orbital.[48,49] Therefore, only three bands are observed for the methoxy group.[5,50]

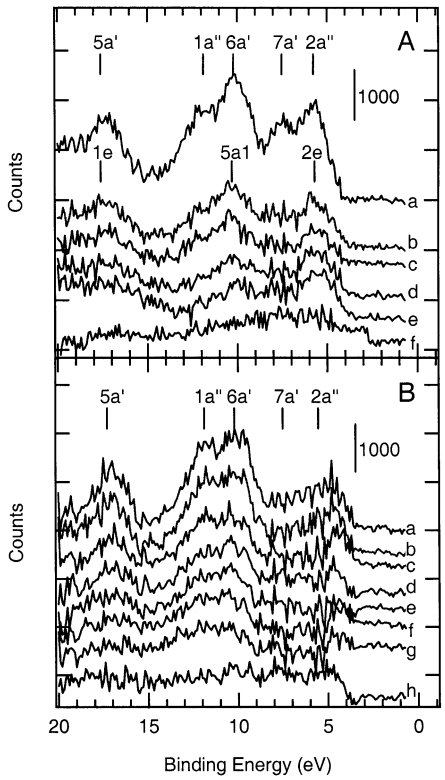

Figure 3. (A) UPS difference spectra following the adsorption of methanol on the reduced WO_3(001) surface at temperatures and absolute coverages of (a) 140 K, 1.5 ML; (b) 186 K, 0.60 ML; (c) 205 K, 0.55 ML; (d) 250 K, 0.27 ML; (e) 310 K; and (f) 500 K. (B) UPS difference spectra following the adsorption of methanol on the oxidized WO_3(001) surface after sputtering at temperatures and coverages of (a) 140 K, 1.1 ML; (b) 160 K, 0.83 ML; (c) 187 K, 0.50 ML; (d) 195 K, 0.42 ML; (e) 205 K, 0.40 ML; (f) 220 K, 0.26 ML; (g) 250 K, 0.12 ML; and (h) 310 K, 0.03 ML. The UPS and corresponding coverage measurements were conducted separately.

UPS difference spectra of methanol adsorption on the WO_3(001) surfaces are shown in Figure 3. Figure 3A shows the spectra for methanol adsorption on the sputtered WO_3 surface as a function of coverage and temperature. For multilayer adsorption, at a coverage of 1.5 ML and 140 K, five peaks are detected at 5.8 eV (2a″), 7.5 eV (7a′), 10.2 eV (6a′), 11.9 eV (1a″), and 17.4 eV (5a′) and are associated with the molecular orbitals of methanol. This observation is consistent with the results for methanol adsorption on the aluminum oxide surface,[5] on Cu(110),[51] and on the aluminum surface,[52] suggesting molecularly adsorbed methanol. However, the five bands evolve into three bands at 5.8 eV (2e), 10.2 eV ($5a_1$), and 17.4 eV (1e), which are assigned to methoxy, for submonolayer adsorption at surface temperatures above 186 K. The decrease in the intensity of the 1a″ peak at 186 K, and a further reduction in intensity at 250 K, suggests that a majority of the methanol dissociates into methoxy on the reduced surface (Figure 3A, spectra b−e). All of the bands disappeared by 500 K.

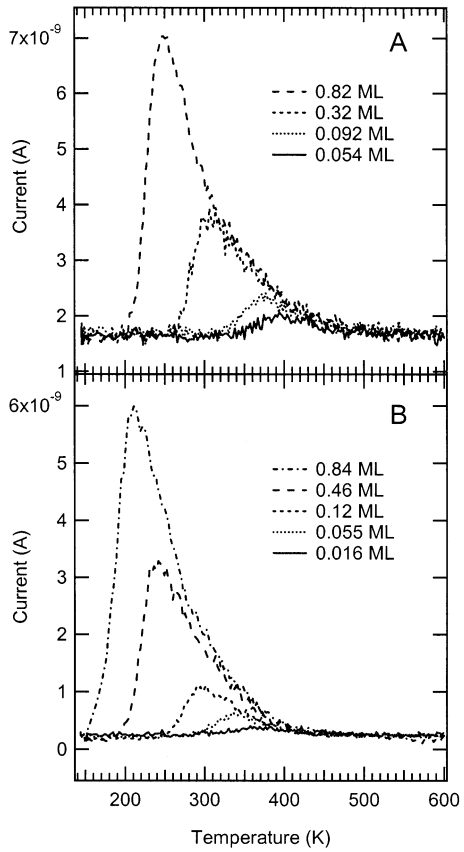

Figure 4. Thermal desorption spectra of methanol (31 amu signal) on (A) the reduced WO_3(001) surface and the (B) oxidized WO_3(001) surface. Dosing of methanol was performed at 140 K through a microarray doser, and the temperature ramp rate was 4 K/s.

UPS spectra for methanol adsorption on the oxidized WO_3 surface are shown in Figure 3B. Four bands can be identified at 5.5, 10.2, 11.8, and 17.1 eV for the multilayer adsorption at 140 K. Compared with the UPS spectra for adsorption on the sputtered surface, the intensity of the peak at 5.5 eV is greatly suppressed, and the band at 7.5 eV due to the lone-pair electrons on the methanol oxygen atom, observed for the reduced surface, cannot be resolved. This phenomenon was also observed for the adsorption of methanol on the zinc-terminated ZnO(0001) surface in a study by Hirschwald and Hofmann,[53] who suggest that the lone-pair electrons on the oxygen atom are strongly perturbed in the adsorption state because of the interaction of the methanol oxygen atom with cation sites. With increasing surface temperature, the UPS spectrum does not change in character. Thus, the UPS spectra for the oxidized surface suggest that methanol adsorbs molecularly both in the multilayer and submonolayer adsorption regimes.

Thermal Desorption of Methanol on WO_3(001) Surfaces. Figure 4 shows coverage-dependent desorption spectra of methanol on the WO_3(001) surfaces. In all of the experiments, the fragmentation pattern agreed with methanol. Although a range of mass fragments were monitored, including 28, 29, and 30 (formaldehyde), 29, 45, and 46 (dimethyl ether), 28 (CO), and 44 (CO_2), no other products were observed. With the sputtered surface, the peak desorption temperature is 390 K for a coverage of 0.054 ML, where 1 monolayer (ML) is defined to be 10^{15} molecules/cm^2, and decreases with increasing surface coverage, as shown in Figure 4A. For the oxidized surface, the desorption temperature is 360 K for a coverage of 0.016 ML and decreases with increasing surface coverage, as shown in Figure 4B. The desorption features of methanol on sputtered and oxidized WO_3 surfaces show similar behavior in that, with increasing coverage, the peak temperature decreases but the high-temperature sides of all of the spectra overlap. Similar spectra have been observed for both single-crystal and polycrystalline oxide surfaces for water[13−15] and methanol.[6,7] This common behavior could be attributed to the desorption process or possibly limitations of the conductance of thermal desorption spectrometers used by a number of groups in studying H_2O and alcohol desorption since these compounds adsorb on the UHV system walls.

Although the mass spectrometer is housed in a separately differentially pumped section of the UHV system and the pumping time constant for inert gases is designed to be 6 ms,[18] the pumping speed for sticky gases is not easy to predict. Therefore, we constructed a viton shutter that could be rotated rapidly into position to close the aperture of the mass spectrometer shroud. Methanol was admitted to the UHV chamber, creating a pressure difference of an order of magnitude between the sample and mass spectrometer housing regions. The shutter was opened and closed, and the mass spectrometer current responded too quickly to measure with the present electronics, placing an upper limit for the methanol pumping time constant at 100 ms. Compared to the 10−25 s width of the desorption curves, the shape is not significantly broadened by the mass spectrometer electronics or differentially pumped housing conductance.

III. B. Theoretical Results. Monte Carlo simulations on homogeneous surfaces have been studied by other groups.[16,17] Because the barrier to diffusion for simple adsorbates is typically 10% of the desorption barrier, most simulations have included a diffusion step to equilibrate the surface between desorption steps. However, experimental evidence for the desorption of H_2O from Al_2O_3(0001) [15] suggests that diffusion can be much slower than desorption on at least some oxide surfaces. Therefore, we investigated the effect of the relative rates of diffusion versus desorption on the coverage-dependent shape of the desorption curves. We focused on desorption from the oxidized surface since UPS shows that methanol is molecularly adsorbed at all coverages and temperatures. Therefore, a first-order molecular desorption process is justified.

The decrease in desorption temperature with increasing coverage, also observed for H_2O on the TiO_2(110) surface,[13] has been interpreted as due to repulsive interactions. However, to achieve a sufficiently large temperature shift at desorption temperatures of 200−400 K, the repulsive interaction causes a splitting at high coverage. The simulation for rapid diffusion and repulsive interactions in the homogeneous surface model, illustrated in Figure 5A, is similar to that in previous studies[16] but is not consistent with the experimental behavior. When diffusion is negligible, the desorption curves show a markedly different character, as shown in Figure 5B. For lower coverage, the peaks tail to lower temperature, but at higher coverage, the additional repulsive interaction between neighbors leads to a second peak. Thus, an evaluation of the repulsive interaction model on a homogeneous surface cannot explain our methanol results and similar data,[3,6,7,13−15] with either rapid or negligible diffusion.

Because we expect hydrogen bonding interactions between methanol molecules (or water) to be attractive, and the case of negligible diffusion has not been previously reported, we compare in Figure 5C and D the cases of rapid and negligible diffusion, respectively. As expected, the desorption peaks shift to higher temperature with increasing coverage, which is qualitatively different from the methanol desorption behavior.

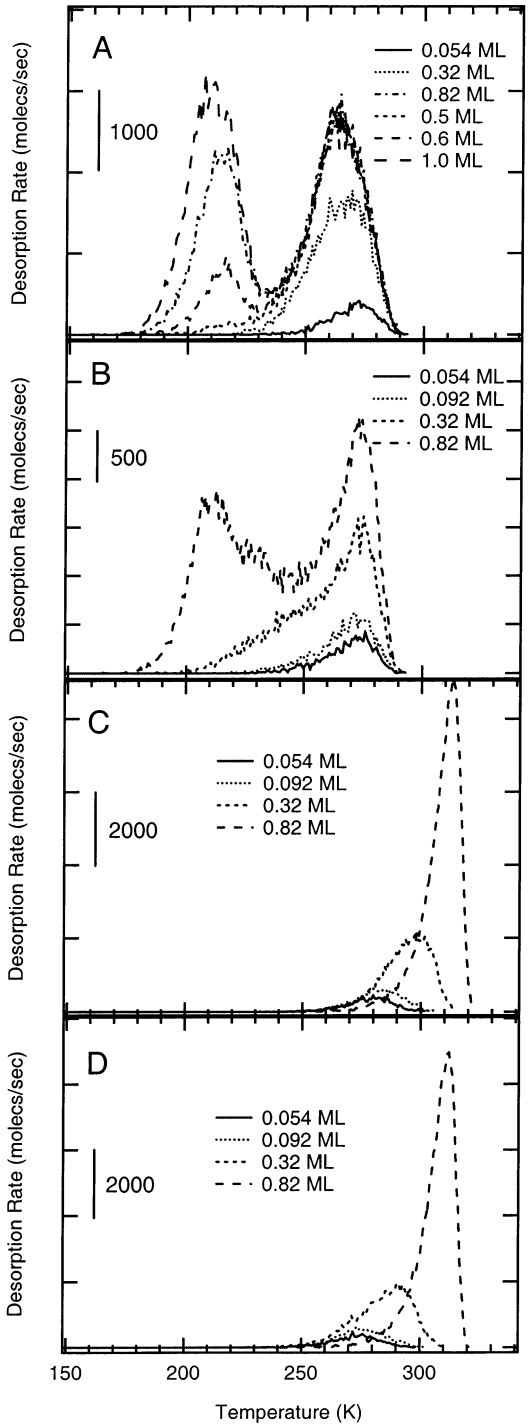

Figure 5. Monte Carlo simulations of molecular desorption on a homogeneous surface at various coverages, as indicated in the panels, with a binding energy of 70 kJ/mol, a ramp rate of 4 K/s, and a preexponential factor of $\nu = 10^{13}$ s^{-1} with (A) rapid surface diffusion and a repulsive interaction of 4 kJ/mol between adsorbates, (B) negligible surface diffusion and a repulsive interaction of 4 kJ/mol between adsorbates, (C) rapid surface diffusion and an attractive interaction of 4 kJ/mol between adsorbates, and (D) negligible surface diffusion and an attractive interaction of 4 kJ/mol between adsorbates.

Note that when diffusion is rapid compared to desorption (Figure 5C) the behavior can also be described by half-order desorption, but for the slow diffusion case, the curves are qualitatively different.

Nelson et al.[15] analyzed their data for H_2O/Al_2O_3(0001) using a distribution of adsorption sites for the case in which the sample was exposed to saturation coverage and then annealed to remove the weaker bound species. We have simulated a distribution of adsorption sites and varied the ratio of the diffusion versus desorption rates. The results show that even relatively low rates of diffusion are sufficient to keep the surface near equilibrium.

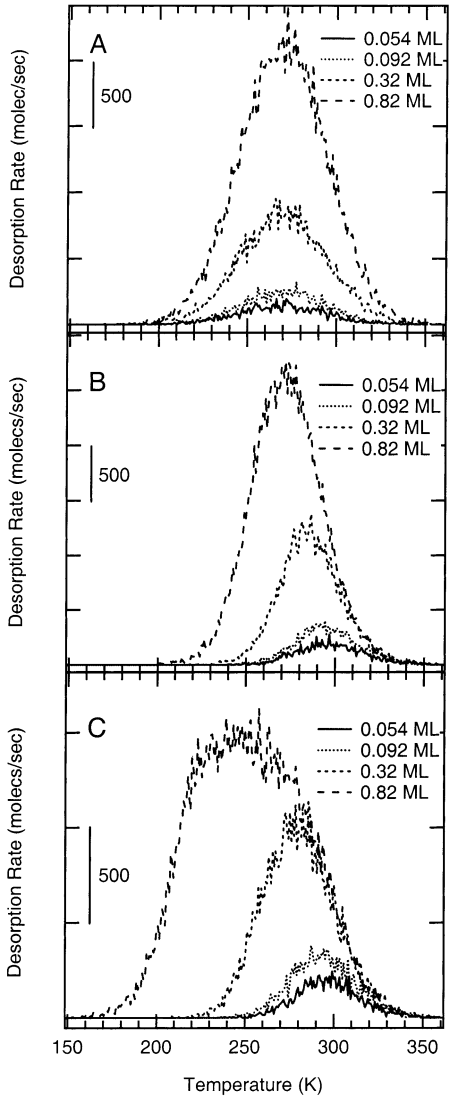

Figure 6. Monte Carlo simulations of the first-order desorption on a heterogeneous surface assuming a normal distribution of the surface sites with a mean of 70 kJ/mol and a standard deviation of 6 kJ/mol, a ramp rate equal to 4 K/s, and a preexponential factor of $\nu = 10^{13}$ s^{-1} for the indicated coverages with (A) negligible surface diffusion and no interactions between adsorbates, (B) negligible interactions between adsorbates but with rapid surface diffusion, and (C) rapid surface diffusion and repulsive interactions of 3 kJ/mol between adsorbates.

Figure 6 shows the results of Monte Carlo simulations of first-order desorption on a heterogeneous surface. The surface site binding energies were described by a normal distribution with an average energy of 70 kJ/mol and a standard deviation of 6 kJ/mol. A temperature ramp rate of 4 K/s and a desorption preexponential factor of $\nu = 10^{13}$ s^{-1} were used. Figure 6A shows the simulation results for increasing surface coverage with both the interactions between adsorbates and surface diffusion negligible. As can be seen, the desorption temperatures do not change with surface coverage, and random population leads to a similar shape for all coverages. By contrast, Figure 6B shows a simulation in which the adsorbate interaction is neglected, but diffusion is sufficiently fast that an equilibrium adsorption state can be established before every desorption event. The simulations with rapid diffusion produce desorption spectra with

overlapping high-temperature tails, which are qualitatively similar to the experimental observations shown in Figure 4. A simulation similar to that in Figure 6B but with a repulsive interaction of 3 kJ/mol is shown in Figure 6C. The repulsive interaction causes the desorption temperature to shift to lower temperature, compared with the results in Figure 6B, but results in a flat-topped or split peak at higher coverage.

If attractive interactions (e.g., hydrogen bonding between adsorbed methanol molecules) are introduced on the heterogeneous surface, then the desorption temperature increases with the coverage as expected (spectra are not shown here). Therefore, a model with an attractive interaction is not compatible with the desorption of methanol on these WO_3 surfaces.

IV. Discussion

IV. A. Adsorption Site and Species. Dixon et al. have studied the electronic states of the single-crystal $WO_3(001)$ surface following treatments of sputtering and annealing using photoelectron spectroscopy combined with STM.[39] The close correspondence between the XPS and UPS spectra for the $WO_3(001)$ surfaces in our study with the data given by Dixon et al., together with the similarity in surface treatments, provides some basis for the structural characterization of our surfaces. On the basis of their STM studies, we are able to associate the reduced surface with the (1×1) structure with most of the terminal oxygen removed and the oxidized surface with the $c(2 \times 2)$ structure with troughs.

Previous studies have revealed that methanol adsorbs on metal oxide surfaces with oxygen bound to coordinatively unsaturated cation sites via lone-pair electrons.[54] On the oxidized surface, the change in intensity of the 7a′ and 2a″ molecular orbitals localized on the oxygen atom (as shown in the UPS spectra of Figure 3) is strong evidence for interaction with a Lewis acid site. The five-coordinate, formally W^{5+} sites of the $c(2 \times 2)$ surface as well as cations in the troughs, whose detailed structure remains unclear, are both possible Lewis acid sites. Our ability to calibrate the desorption spectrum and give absolute coverages allows us to determine that a large majority of exposed cation sites on the oxidized surface act as Lewis acid sites. Noting that the coverage of methanol in Figure 3B, curves a and b, is a full monolayer and yet the emission from the 7a′ and 2a″ molecular orbitals remains suppressed shows not only that trough sites may act as Lewis acid sites but also that the majority of $c(2 \times 2)$ sites must be relatively strong Lewis acid sites. The presence of strong Lewis acid sites on dehydroxylated, high surface area WO_3 powders has also been found by work in our laboratory by the Tripp group, using pyridine as a probe molecule.[55]

Despite evidence for strong Lewis acid sites, we found that dissociation did not occur on the oxidized surface. Dissociation of this weak Brønsted acid requires a pair of acid/base sites in which a lattice oxygen atom acts as the Brønsted base site. Both bridging and terminal oxygen atoms are possible Brønsted base sites. The inactivity of the oxidized surface implies that the basicity of the surface oxygen is too low to dissociate the hydroxyl group. Some evidence supporting this argument can be found in the study of the adsorption of H_2O on the $Na_xWO_3(001)$ surface using HREELS.[56] It was found that water molecularly adsorbed on the tungsten bronze (001) surface with the oxygen end bonded to the tungsten cation, but no dissociation was detected. Since water has a significantly higher acidity than methanol, we can conclude that the oxidized surface has only weak Brønsted acid sites.

This observation can be understood from the surface structure of the oxidized surface. The five-coordinate W^{5+} sites comprise the majority of adsorption sites on the oxidized surface for methanol; therefore, the bridging oxygen is the closest potential Brønsted base site. However, the bridging oxygen is bonded to two tungsten cations, decreasing the electron density on the bridging oxygen and resulting in weak Coulombic interactions with the hydroxyl hydrogen. As far as the terminal oxygen is concerned, its large distance from the Lewis acid adsorption site may present a prohibitively large barrier to dissociation. The tungsten−tungsten spacing is around 3.7 Å, which can be compared qualitatively to the maximum oxygen−oxygen distance for effective hydrogen bonding of 3.5 Å.[57,58]

By contrast, the UPS data clearly shows that on the reduced surface the large majority of methanol adsorbs dissociatively. If the W 4f XPS spectra are interpreted within the final-state model to imply that only W^{5+} sites exist on the (1×1) surface, as proposed by Jones et al.,[59] then the higher electron density on the surface (as revealed by a larger intensity in the gap in UPS measurements[39]) suggests an increase in the basicity of the bridging oxygens relative to that of the oxidized surface. Theoretical calculations regarding the electronic structure of the reduced surface are needed to understand the dissociation mechanism fully.

Although we prefer the final-state interpretation of the W 4f XPS region to the initial-state model (see below), we are not aware of independent evidence to exclude the presence of lower oxidation state species and in particular metallic tungsten species. The presence of metallic tungsten could also account for the dissociative adsorption of methanol on the reduced surface. However, the decomposition of methanol on tungsten, and other metal surfaces, results in the production of H_2 and CO.[60,61] During CTDS experiments, we did not detect any H_2, CO, or CO_2 desorption. Nevertheless, we cannot completely exclude the possibility of small metallic tungsten clusters, since the behavior of clusters may differ significantly from the reactivity of a metal surface.

IV. B. Roles of Diffusion and Surface Heterogeneity. The experimental data of Figure 4 cannot be explained by intermolecular interactions on a homogeneous surface, either with or without rapid diffusion. Repulsive interactions lead to peak splitting, and attractive interactions shift the peak to higher temperature with increasing coverage. Qualitatively, the heterogeneous surface model, shown in Figure 6B, is consistent with the coverage dependence of the spectra on the oxidized surface (Figure 4B), and the overlap of the high-temperature side of the peaks indicates that diffusion is rapid compared to desorption. Further refinement of the lattice site adsorption energy distribution could be performed to more closely fit the experimental data, as done by Nelson et al.;[15] however, the results would not provide fundamental information in our case without more extensive characterization of the surface structure and morphology.

The origin of the surface heterogeneity, necessary to explain the coverage-dependent spectra, is most likely associated with the surface structure of the epitaxial films. Experimentally, it was found that the $WO_3(001)$ surface is characterized by stepped structures.[32] Sputtering preferentially removes oxygen and generates oxygen vacancy defects, as revealed by the XPS spectra. Nevertheless, similar desorption behavior was observed in the desorption of H_2O from a hydroxylated α-$Al_2O_3(0001)$ surface by Nelson et al,[15] in which the single-crystal surface was known to be nearly defect-free prior to desorption. The independence of the peak shape and position with increasing dose suggests that mobility is poor. Thus, the heterogeneity of

the surface seems to arise during the dehydroxylation process, not from the initial surface defect structure.

The simulation results imply that neither repulsive nor attractive interactions, and in particular hydrogen bonding, contribute significantly to the coverage and temperature dependence of methanol desorption from the reduced and oxidized surfaces. Although this seems surprising, the formation of an effective hydrogen bond requires an oxygen−oxygen distance less than 3.5 Å.[57,58] For the adsorption of methanol on WO_3 surfaces, with molecular adsorption at the tungsten cation (Lewis acid) sites, the tungsten−tungsten spacing of approximately 3.7 Å[33] is not very favorable for hydrogen bond formation. Furthermore, molecular dynamics studies of hydrogen bonding in crystalline and liquid-phase methanol suggest that hydrogen bonding can occur only with two nearest neighbors, forming either 1D chains or cyclic chains, which further reduces the possible role of hydrogen bonding[62−64] in the desorption energetics.

The UPS spectra showed that the methanol adsorbed molecularly on the oxidized surface and dissociatively on the reduced surface. However, the coverage-dependent desorption spectra for methanol on both surfaces are qualitatively very similar, as shown in Figure 4. The main difference is that desorption occurs at higher temperatures on the reduced surface. This implies that desorption from the reduced surface is essentially a pseudo-first-order process. The reasons for this are not easily justified. Such behavior is found for the desorption of H_2 from the dissociatively adsorbed hydride state on the Si(100) dimers.[65] The first-order behavior in the silicon hydride case is thought to be due to the poor mobility of the hydride species and that the close proximity of the two hydrides leads to a concerted desorption process. Although the simulation shows clearly that the diffusion of *methanol* on the *oxidized* surface is relatively fast compared to desorption, this does not necessarily imply that the *methoxy* species is mobile on the *reduced* surface.

As discussed above, the dissociation of methanol probably requires a local acid/base pair site configuration favorable for dissociation of the hydroxyl group. A highly mobile methanol precursor state could then dissociate at a strong Brønsted base site, which retains the proton in close proximity to a more strongly bound methoxy group. The assumption that a stronger Lewis acid/Brønsted base site pair is required for the dissociation of methanol is supported by the higher desorption temperature of methanol on the reduced surface. Thus, the methoxy can desorb in a pseudo-first-order process as methanol by combining with the neighboring proton.

IV. C. Reaction Mechanism on the Reduced Surface. During the CTDS experiments, both on the reduced and oxidized WO_3(001) surfaces, methanol is the only desorption product detected. By comparison, methanol was found to react on the sputtered and annealed TiO_2(001) surface to form dimethyl ether.[3] Adsorbate surface mobility and the adsorption structure were thought to be the key factors in facilitating the surface coupling reaction. Kim and Barteau[3] proposed that the doubly coordinatively unsaturated site is the active center responsible for dimethyl ether formation on TiO_2(001) single-crystal surfaces, resulting in the close proximity of two adsorbed methoxy groups. This argument was based on the fact that dimethyl ether was detected only on the {114}-facetted surface, which was characterized by the stepped structure containing 4-fold oxygen coordination sites and not on the {011}-facetted surface, which is characterized by a 5-fold oxygen coordination structure. If the reduced surface is characterized by a (1×1) structure with most of the terminal oxygens removed, then the large tungsten−tungsten distance would not favor the coupling reaction. However, the interpretation of the coverage-dependent desorption spectra suggests that adsorbate mobility is not the limiting factor for dimethyl ether production.

A closer tungsten−tungsten distance can, however, be achieved at shear plane structures. During sputtering and annealing, the removal of lattice oxygen can also lead to the conversion of corner-sharing octahedra into edge-sharing structures, as found in the bulk at crystallographic shear (CS) planes.[66] Experimentally, the formation of the CS plane was a facile route for the oxidation of the allyl group to acrolein on reduced WO_3 surfaces.[67] Although we find that the decomposition of dimethyl methyl phosphonate (DMMP) on the reduced surface produces dimethyl ether, the fact that dimethyl ether was not observed in this study, from the dissociatively adsorbed methoxy groups, eliminates the possible role of these sites for a surface-mediated coupling reaction.

IV. D. Interpretation of XPS Data. The W 4f region of the XPS spectra of Figure 2 could be interpreted in at least three different ways. The initial-state model, involving W^{6+}, W^{5+}, W^{4+}, and W^0 species, could be justified on the basis of apparent binding energies of reference compounds. The presence of the W^{6+} species is easily understood in terms of fully octahedrally coordinated cations, whereas the W^{5+} sites could be ascribed either to the cations in the c(2×2) structure with missing terminal oxygens or to cations along idealized shear plane structures. The assignment of the W^{4+} species is less clear but could be attributed either to cations along shear planes that are missing terminal oxygens or to regions of WO_2. The reduction of WO_3 to WO_2 is thought to be unlikely under vacuum reduction conditions, according to X-ray diffraction experiments.[68] However, we are not aware of any other independent evidence for the formation of W^0 under the conditions of the experiment, and the reactivity toward methanol, as noted above, is not typical of tungsten metal.

The interpretation of the spectra in terms of final-state screening effects, consistent with that of Dixon et al.,[39] is in good agreement with other information we have regarding the properties of our epitaxial films. First, comparing the splitting between the screened and unscreened final-state levels to the empirical data given by Chazalviel et al.[42] for a range of sodium bronzes, the substoichiometry, x, in our WO_{3-x} films would be approximately 0.05. Second, the relative intensity in the gap to that in the valence-band region, again according to a theoretical relation given by Chazalviel et al.,[42] predicts a substoichiometry of a few percent. Third, the ratio, β, of the intensity of the unscreened final-state feature to that of the screened final state was found empirically to behave as $\beta = 0.75x^{-1/3}$ by Chazalviel et al.,[42] which predicts ratios between 2 and 3.5 for $x = 0.05$ and 0.01, respectively, which is consistent with the fits shown in Figure 2. Measurements of the optical absorbance of our epitaxial films in the UV−vis region and estimates of the carrier concentration and mobility give values for the substoichiometry in the range of 0.01 to 0.05, depending upon the growth and operating conditions of the films in sensor applications.[35,69] Thus, the presence of a screened final state for the reduced surface seems to be consistent with the carrier density in these materials.

On general grounds, Occam's razor would suggest that if the data can be fit with fewer doublets then the simpler model should be chosen (i.e., fewer doublets are required in the final-state model). However, the interpretation of Dixon et al.[39] implies a spatial localization of the narrow bands. In the case

of sodium bronze, only one (formally W^{6+}) initial state was considered, and the presence of two features originated from the screened or unscreened final states. If the electrons produced from the reduction of WO_3 form a narrow band that is delocalized, similarly to the sodium bronze, then there should be *four* doublets in the W 4f region, two originating from each initial state (formally W^{6+} and W^{5+}). If the W^{6+} initial states result only in one unscreened final state, then the implication is that the narrow band must be spatially localized to regions, such as the high tunneling probability "bright rafts" in which there are (formally) W^{5+} sites. Further systematic work, particularly on well-characterized surfaces in which the electron density can be estimated, for example, from the plasmon frequency with HREELS, is required to resolve this issue.

V. Conclusions

We have prepared two types of WO_3(001) surfaces, referred to as oxidized and reduced, that are characterized by strong Lewis acid sites in which the terminal oxygen is removed, leading to tungsten cations, in a formally 5+ or 4+ oxidation state. On the oxidized surface, UPS shows that methanol bonds molecularly to Lewis sites, whereas on the reduced surface, stronger Brønsted base sites lead to dissociative adsorption.

The coverage-dependent desorption of methanol shows strong shifts to lower temperature, similar to the behavior of water and other alcohols on oxide surfaces. Monte Carlo simulations allow the relative importance of diffusion and desorption to be assessed from coverage-dependent spectra. Qualitatively different behavior is also found for the effects of a heterogeneous surface and intermolecular interactions for both the cases of slow and rapid diffusion. On WO_3, the diffusion of molecular methanol is relatively rapid. The structural constraints of the large tungsten−oxygen−tungsten cation distances appear to prevent significant hydrogen bonding between adsorbed methanol molecules. Thus, the coverage dependence of the desorption spectra is attributed to the heterogeneity of the adsorbate−surface interaction.

Acknowledgment. We acknowledge helpful discussions with Robert Jackson regarding the calibration of the CTDS system and George Bernhardt for the growth of WO_3 films on the sapphire substrates. This work was sponsored by the Department of the Navy, Naval Surface Warfare Center, Dahlgren Laboratory, Grant No. N00178-99-1-9002 and the Office of Naval Research Grant No. N00014-01-1-0921.

References and Notes

(1) Christmann, K. *Introduction to Surface Physical Chemistry*; Springer-Verlag: New York, 1991.
(2) Vohs, J. M.; Barteau, M. A. *Surf. Sci.* **1986**, *176*, 91−114.
(3) Kim, K. S.; Barteau, M. A. *Surf. Sci.* **1989**, *223*, 13−32.
(4) Cox, D. F.; Schulz, K. H. *J. Vac. Sci. Technol., A* **1990**, *8*, 2599.
(5) Frederick, B. G.; Apai, G.; Rhodin, T. N. *Surf. Sci.* **1992**, *277*, 337−350.
(6) Gercher, V. A.; Cox, D. F.; Themlin, J. M. *Surf. Sci.* **1994**, *306*, 279−293.
(7) Nishimura, S. Y.; Gibbons, R. F.; Tro, N. J. *J. Phys. Chem. B* **1998**, *102*, 6831−6834.
(8) Wong, G. S.; Kragten, D. D.; Vohs, J. M. *Surf. Sci.* **2000**, *452*, L293−L297.
(9) Schildbach, M. A.; Hamza, A. V. *Surf. Sci.* **1993**, *282*, 306−322.
(10) Hugenschmidt, M. B.; Gamble, L.; Campbell, C. T. *Surf. Sci.* **1994**, *302*, 329−340.
(11) Gercher, V. A.; Cox, D. F. *Surf. Sci.* **1995**, *322*, 177−184.
(12) Akbulut, M.; Sack, N. J.; Madey, T. E. *Surf. Sci.* **1996**, *351*, 209−227.
(13) Henderson, M. A. *Surf. Sci.* **1996**, *355*, 151−166.
(14) Stirniman, M. J.; Huang, C.; Smith, R. S.; Joyce, S. A.; Kay, B. D. *J. Chem. Phys.* **1996**, *105*, 1295.
(15) Nelson, C. E.; Elam, J. W.; Cameron, M. A.; Tolbert, M. A.; George, S. M. *Surf. Sci.* **1998**, *416*, 341−353.
(16) Meng, B.; Weinberg, W. H. *J. Chem. Phys.* **1994**, *100*, 5280.
(17) Weinketz, S. *J. Chem. Phys.* **1994**, *101*, 1632.
(18) Jackson, R. H. Spatial Distributions and Transient Fluxes in Calibrated Thermal Desorption Spectroscopy. Ph.D. Dissertation, University of Maine, Orono, ME, 2000.
(19) Sundberg, M.; Tilley, R. J. D. *J. Solid State Chem.* **1974**, *11*, 150.
(20) Salje, E.; Carley, A. F.; Roberts, M. W. *J. Solid State Chem.* **1979**, *29*, 237.
(21) Bringans, R. D.; Hochst, H.; Shanks, H. R. *Phys. Rev. B* **1981**, *24*, 3481.
(22) Jones, F. H.; Rawlings, K.; Foord, J. S.; Cox, P. A.; Egdell, R. G.; Pethica, J. B.; Wanklyn, B. M. R. *Phys. Rev. B* **1995**, *52*, R14392.
(23) Pilling, R. S.; Bernhardt, G.; Frederick, B. G. To be submitted for publication.
(24) Pilling, R. S.; Bernhardt, G.; Kim, C. S.; Duncan, J.; Crothers, C. B. H.; Kleinschmidt, D.; Frankel, D. J.; Lad, R. J.; Frederick, B. G. *Sens. Actuators, B*, submitted for publication.
(25) Kim, C. S.; Lad, R. J.; Tripp, C. P. *Sens. Actuators, B* **2001**, *76*, 442−448.
(26) Templeton, M. K.; Weinberg, W. H. *J. Am. Chem. Soc.* **1985**, *107*, 97−108.
(27) Henderson, M. A.; Jin, T.; White, J. M. *J. Phys. Chem.* **1986**, *90*, 4607−4611.
(28) Li, Y.; Klabunde, K. J. *Langmuir* **1991**, *7*, 1388−1393.
(29) Mitchell, M. B.; Sheinker, V. N.; Mintz, E. A. *J. Phys. Chem. B* **1997**, *101*, 11192−11203.
(30) Rusu, C. N.; J. T. Yates, J. *J. Phys. Chem. B* **2000**, *104*, 12292−12298.
(31) Ma, S.; Jackson, R. L.; Frederick, B. G. To be submitted for publication.
(32) Moulzolf, S. C.; LeGore, L. J.; Lad, R. J. *Thin Solid Films* **2001**, *400*, 56−63.
(33) LeGore, L. J.; Lad, R. J.; Moulzolf, S. C.; Vetelino, J. F.; Frederick, B. G.; Kenik, E. A. *Thin Solid Films* **2002**, *406*, 79−86.
(34) Scofield, J. H. *J. Electron Spectrosc. Relat. Phenom.* **1976**, *8*, 129−137.
(35) Moulzolf, S. C.; Ding, S. A.; Lad, R. J. *Sens. Actuators, B* **2001**, *77*, 375−382.
(36) Woodward, P. M.; Sleight, A. W.; Vogt, T. *J. Phys. Chem. Solids* **1995**, *56*, 1305.
(37) *JCPDS Diffraction Tables*; JCPDS, Ed.; International Centre for Diffraction Data: Newton, PA, 1997.
(38) Tanner, R. E.; Meethunkij, P.; Altman, E. I. *J. Phys. Chem. B* **2000**, *104*, 12315−12323.
(39) Dixon, R. A.; Williams, J. J.; Morris, D.; Rebane, J.; Jones, F. H.; Egdell, R. G.; Downes, S. W. *Surf. Sci.* **1998**, *399*, 199−211.
(40) Jones, F. H.; Rawlings, K.; Foord, J. S.; Egdell, R. G.; Pethica, J. B.; Wanklyn, B. M. R.; Parker, S. C.; Oliver, P. M. *Surf. Sci.* **1996**, *359*, 107−121.
(41) Friedel, J. *Comments Solid State Phys.* **1969**, *2*, 21.
(42) Chazalviel, J. N.; Campagna, M.; Wertheim, G. K.; Shanks, H. R. *Phys. Rev. B* **1977**, *16*, 697.
(43) Kim, K. S.; Baitinger, W. E.; Amy, J. W.; Winograd, N. *J. Electron Spectrosc. Relat. Phenom.* **1974**, *5*, 351.
(44) Angelis, B. A. D.; Schiavello, M. *J. Solid State Chem.* **1977**, *21*, 67−72.
(45) Sabbatini, L.; Sherwood, P. M. A.; Zambonin, P. G. *J. Electrochem. Soc.* **1983**, *130*, 2199.
(46) Wong, H. Y.; Ong, C. W.; Kwok, R. W. M.; Wong, K. W.; Wong, S. P.; Cheung, W. Y. *Thin Solid Films* **2000**, *376*, 131.
(47) Jorgensen, W. L.; Salem, L. *The Organic Chemist's Book of Orbitals*; Academic Press: New York, 1973.
(48) Erskine, J. L.; Bradshaw, A. M. *Chem. Phys. Lett.* **1980**, *72*, 260.
(49) Rodriguez, J. A. *Surf. Sci.* **1992**, *273*, 385.
(50) Bowker, M.; Madix, R. J. *Surf. Sci.* **1982**, *116*, 549−572.
(51) Bowker, M.; Madix, R. J. *Surf. Sci.* **1980**, *95*, 190−206.
(52) Rogers, J. W., Jr.; Hance, R. L.; White, J. M. *Surf. Sci.* **1980**, *100*, 388−406.
(53) Hirschwald, W.; Hofmann, D. *Surf. Sci.* **1984**, *140*, 415−424.
(54) Onishi, H.; Aruga, T.; Egawa, C.; Iwasawa, Y. *Surf. Sci.* **1988**, *193*, 33−46.
(55) Kanan, S. M.; Lu, Z.; Cox, J. K.; Bernhardt, G.; Tripp, C. P. *Langmuir* **2002**, *18*, 1707.
(56) Aitken, D. G.; Cox, P. A.; Egdell, R. G.; Hill, M. D.; Sach, I. *Vacuum* **1983**, *33*, 753−756.
(57) Sarkar, S.; Joarder, R. N. *J. Chem. Phys.* **1993**, *99*, 2032.
(58) Lindan, P. J. D.; Harrison, N. M. *Phys. Rev. Lett.* **1998**, *80*, 762.
(59) Jones, F. H.; Dixon, R. A.; Brown, A. *Surf. Sci.* **1996**, *369*, 343−350.
(60) Egelhoff, W. F.; Perry, D. L.; Linnett, J. W. *J. Electron Spectrosc. Relat. Phenom.* **1974**, *5*, 339−350.

(61) Egelhoff, W. F.; Linnett, J. W.; Perry, D. L. *Faraday Discuss. Chem. Soc.* **1975**, *60*, 127.
(62) Allan, D. R.; Clark, S. J.; Brugmans, M. J. P.; Ackland, G. J.; Vos, W. L. *Phys. Rev. B* **1998**, *58*, R11 809.
(63) Asahi, N.; Nakamura, Y. *Chem. Phys. Lett.* **1998**, *290*, 63.
(64) Bako, I.; Jedlovszky, P.; Palinkas, G. *J. Mol. Liq.* **2000**, *87*, 243.
(65) Wise, M. L.; Koehler, B. G.; Gupta, P.; Coon, P. A.; George, S. M. *Surf. Sci.* **1991**, *258*, 166.
(66) Bursill, L. A.; Hyde, B. G. *J. Solid State Chem.* **1972**, *4*, 430−446.
(67) Haber, J.; Janas, J.; Schiavello, M.; Tilley, R. J. D. *J. Catal.* **1983**, *82*, 395−403.
(68) Booth, J.; Ekstrom, T.; Iguchi, E.; Tilley, R. J. D. *J. Solid State Chem.* **1982**, *41*, 293−307.
(69) Ren, H. Current Voltage Characteristics of a Semiconductor Metal Oxide Sensor. M.S. Thesis, University of Maine, Orono, ME, 2001.